Industrial Chemistry & Materials

ROYAL SOCIETY OF CHEMISTRY

PAPER

View Article Online
View Journal

Cite this: DOI: 10.1039/d5im00286a

Open Access Article. Published on 26 1404. Downloaded on 09/03/1405 12:12:44 .
This article is licensed under a Creative Commons Attribution-NonCommercial 3.0 Unported Licence.

Naphthalimide-based nonionic sulfonate photoacid generators: structure–property relationship and sub-30 nm resolution lithography

Changchang Zhuang, †[a] Jiao Chen,†[a] Tao Wang,[a] Jun Zhao,[b] Haoyuan Li, [a] Hanshen Xin *[a] and Jianhua Zhang *[a]

This study reports the design and synthesis of five novel nonionic photoacid generators (PAGs) based on a naphthalimide–benzenesulfonate backbone. Comprehensive evaluations were conducted to assess their solubility, thermal stability, photophysical properties, acid generation quantum yields (Φ_a), and lithographic performance. Ultraviolet-visible (UV-vis) spectroscopy revealed that the optical properties of the PAGs could be finely tuned through structural modifications, with all compounds exhibiting strong absorption at key lithographic wavelengths (248, 254, and 365 nm). Measurements of Φ_a ranged from 6.2% to 17.6%, establishing clear structure–property relationships. Notably, PAG **1d** exhibited the highest Φ_a (17.6%) due to its optimal donor–π–acceptor (D–π–A) configuration, where the synergistic combination of electron-donating and electron-withdrawing groups enhanced photosensitivity and facilitated efficient acid release. Density functional theory (DFT) calculations corroborated these findings, confirming that the established structure–property relationships provide a robust foundation for the molecular engineering of PAGs with high Φ_a. When formulated into photoresists, all PAGs produced high-quality patterning across multiple lithographic platforms, including i-line (365 nm), deep-UV (254 nm), and electron-beam lithography (EBL), with their sensitivity directly correlating to the Φ_a of the PAGs. Remarkably, the PR-**1d** formulation exhibited exceptional performance in EBL, attaining the highest sensitivity (E_0 = 54.4 μC cm^{-2}) and a high resolution of 28 nm, thereby establishing its potential for sub-30 nm lithography applications. This work provides fundamental insights into the structure–property relationships of nonionic sulfonate PAGs and advances resist technology for next-generation lithography.

Received 9th October 2025,
Accepted 17th November 2025

DOI: 10.1039/d5im00286a

rsc.li/icm

Keywords: Nonionic photoacid generators; Naphthalimide-benzenesulfonate; Acid generation quantum yield; Structure–property relationship; Sub-30 nm lithography.

1 Introduction

With the continuous advancement of lithography processes, the demands for the resolution and sensitivity of photoresists are gradually increasing.[1–6] The chemically amplified photoresist (CAR) developed by Ito *et al.*[7–9] significantly enhances the efficiency of photochemical reactions, effectively addressing the challenge of high sensitivity faced by photoresists. The CAR system consists of polymer resins, PAGs, basic quenchers, solvents, and other additives.[10–12] During the exposure process, the PAGs in the photoresist formulation undergoes photolysis to generate acid. In the subsequent post-exposure baking process, acid-catalyzed transformations of polymer functional groups (such as depolymerization, intramolecular dehydration, crosslinking, and deprotection of acidic groups) lead to changes in the polarity and solubility of the polymer. After the catalytic reaction is completed, the released acid continues to catalyze the chain reaction.[13–18] A small amount of PAGs can catalyze the entire chemical reaction of the photoresist, greatly reducing the required exposure dose and significantly increasing the sensitivity of the photoresist, making it an indispensable material in CARs.

From a structural perspective, PAGs can be categorized into ionic and nonionic types. Ionic PAGs, such as sulfonium and iodonium salts, were the workhorses in the early development of CARs, owing to their high thermal stability and the ability to modulate acid strength through selection of counter anions.[19–22] However, their application is often limited by the

[a] *School of Microelectronics, Shanghai Engineering Research Center for Integrated Circuits and Advanced Display Materials, Shanghai University, Shanghai, China. E-mail: xinhanshen@shu.edu.cn, jhzhang@oa.shu.edu.cn*
[b] *Shanghai Synchrotron Radiation Facility, Shanghai Advanced Research Institute, Chinese Academy of Sciences, Shanghai, China*
† These authors contributed equally.

© 2025 The Author(s). Co-published by the Institute of Process Engineering, Chinese Academy of Sciences and the Royal Society of Chemistry

Open Access Article. Published on 26 1404. Downloaded on 09/03/1405 12:12:44 .
This article is licensed under a Creative Commons Attribution-NonCommercial 3.0 Unported Licence.

need for thicker films to achieve sufficient radiation absorption, a suboptimal out-of-band response, and solubility issues in certain formulations, which can adversely affect imaging performance.[23–25] In contrast, nonionic PAGs, typically derived from arylsulfonates, exhibit superior solubility in organic solvents. They are also characterized by a broad absorption spectrum, straightforward synthesis, and ease of purification. These advantages collectively make them highly attractive for applications in photoresists and polymer photoinitiation.[26–33] The core performance parameter for any PAG is acid generation quantum yields (Φ_a), which directly govern photoresist sensitivity. Simultaneously, the photoluminescence quantum yield (Φ_p) acts as a key competitive parameter; it reflects the extent to which excited-state energy is dissipated *via* radiation, thereby intrinsically reducing Φ_a.[34–36] Beyond these, PAG performance is co-determined by several additional key parameters, including absorption characteristics (such as maximum absorption wavelength (λ_{max}) and molar extinction coefficient (ε)), thermal stability, and compatibility with the photoresist matrix. For nonionic PAGs, molecular structure design plays a decisive role in precisely tuning these parameters and optimizing overall performance. Sulfonate ester PAGs based on the naphthalimide backbone have attracted widespread attention over the past decade due to their high stability, good solubility, and efficient acid generation capability.[34,37–41] Previous studies have shown that in such nonionic naphthalimide-based sulfonate ester PAGs, the structure of substituent groups on the sulfonate ester unit plays an important role in regulating Φ_a.[23,36,42] However, the constitutive relationship between the type of functional groups (*e.g.*, electron-donating and electron-withdrawing groups) on the naphthalimide backbone and the Φ_a has not been systematically investigated. Deeper insight in this regard is essential for the rational design of next-generation high-performance PAGs. Furthermore, although nonionic PAGs have been extensively studied and applied in deep ultraviolet (DUV) lithography, their adoption in more advanced sub-30 nm lithography nodes has not been extensively documented and presents new challenges and opportunities that warrant further exploration.

Here, we designed and synthesized five nonionic sulfonate ester PAGs (**1a–e**) based on the naphthalimide backbone. By individually adjusting the electronegativity of the substituent groups on the naphthalimide units and the benzene sulfonate units, we altered the frontier molecule orbital (FMO) energies of the PAGs to regulate their acid generation capabilities. Rhodamine B (RB) was used as an acid indicator, and the acid generation ability of the PAGs was determined *via* UV-visible spectrophotometry. Additionally, we performed theoretical calculations on the PAGs to further understand the relationship between their structure, FMO energy, and acid generation efficiency. These PAGs were subsequently mixed with a polymer (a laboratory-synthesized resin PG, poly(2-phenyl-2-propyl methyl methacrylate-*co*-γ-butyrolactone methyl methacrylate))[43] to prepare the photoresists. The lithographic performance of these photoresists was evaluated using 365 nm and 254 nm UV exposure, as well as EBL. The results indicated that by independently adjusting the electron-donating/withdrawing abilities of the substituent groups on the naphthalimide units and the benzene sulfonate units, it is indeed possible to regulate the acid generation capacity of the PAGs, thereby tuning the sensitivity of the photoresists. As shown in Fig. 1, reducing the electron-donating ability of the substituents at the 4-position on the naphthalimide backbone gradually decreased the acid quantum yield of the PAG molecules. Conversely, increasing the electron-withdrawing ability of the substituents at the *para*-position on the benzene sulfonate units gradually enhanced the acid quantum yield of the PAG molecules. Consequently, PAG **1d**, which possesses electron-donating groups at the 4-position on the naphthalimide backbone and electron-withdrawing groups at the *para*-position on the benzene sulfonate units, exhibited the highest Φ_a (17.6%). All five PAG-based photoresists produced high-quality patterns on various lithographic platforms (365 nm, 254 nm, and EBL), with their sensitivity directly related to their Φ_a values. Furthermore, the photoresist based on PAG **1d** exhibits highly competitive

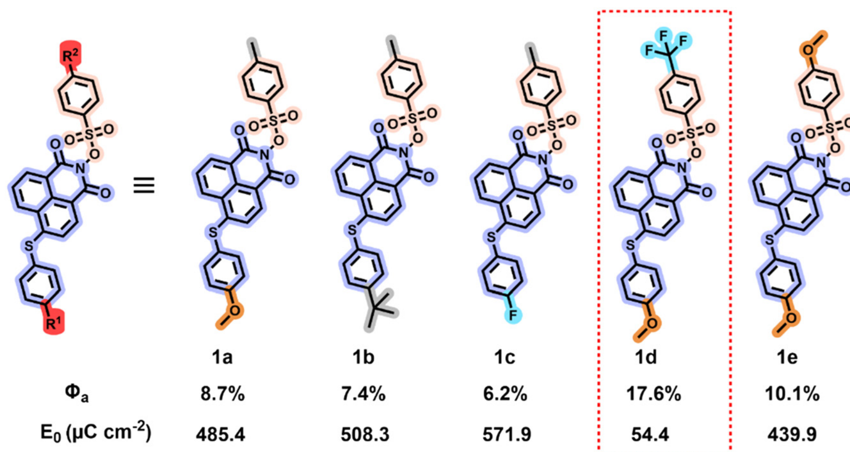

Fig. 1 Molecular structures of PAGs **1a–1e** with Φ_a and EBL E_0 in photoresist formulations.

© 2025 The Author(s). Co-published by the Institute of Process Engineering, Chinese Academy of Sciences and the Royal Society of Chemistry

Open Access Article. Published on 26 1404. Downloaded on 09/03/1405 12:12:44 ..
This article is licensed under a Creative Commons Attribution-NonCommercial 3.0 Unported Licence.

performance, achieving a combination of the highest E_0 (54.4 μC cm^{-2}), high resolution (28 nm), and low line edge roughness (LER = 1.3 nm) under EBL among reported photoresists employing nonionic PAGs.[31,44,45]

2 Results and discussion

2.1 Synthesis and characterization of nonionic sulfonate ester PAGs 1a–1e

The designed nonionic sulfonate ester PAGs **1a–1e** can be synthesized through a three-step reaction sequence, as depicted in Scheme 1. First, substituted phenylthiol derivatives (**S1a–S1c**) bearing different 4-position functional groups undergo a substitution reaction with 4-bromo-1,8-naphthalenedicarboxylic anhydride (**S2**) under alkaline conditions at 75 °C to generate intermediates **S3a–S3c**. Without isolation, intermediates **S3a–c** are then treated with hydroxylamine aqueous solution to afford 4-substituted *N*-hydroxy-1,8-naphthalenedicarboximide derivatives **S4a–c**. The resulting **S4a–c** intermediates, without further purification, subsequently react with substituted benzene sulfonyl chlorides to yield the corresponding naphthalene dicarboximide benzene sulfonate esters **1a–1e**. The three-step synthesis achieves overall yields of 83.6–91.2%. The chemical structures of PAGs **1a–1e** were fully characterized by ^{1}H and ^{13}C NMR spectroscopy, and high-resolution mass spectrometry. Detailed experimental procedures and characterization data for all PAGs can be found in the SI (Fig. S1–S17). This synthetic route adheres to the principles of green chemistry. It utilizes commercially available starting materials, demonstrates excellent atom economy and scalable process potential, and requires no precious metal catalysts or highly polluting reagents throughout the entire process. The fluorination-free/low-fluorine PAG system constructed based on this strategy avoids the use of persistent pollutants such as perfluorooctane sulfonate (PFOS) at the molecular design source, and its non-ionic sulfonate ester architecture also exhibits good environmental stability.

2.2 Solubility

Table S1 summarizes the solubility of PAGs **1a–1e** in commonly used solvents. These compounds exhibit good solubility in non-protonic polar solvents (*e.g.*, DMF) and moderate-polarity solvents (*e.g.*, DCE, 1,4-dioxane, and THF). However, they show comparatively poor solubility in highly polar or protonic solvents such as methanol and acetonitrile. This reduced solubility may be attributed to the presence of multiple aromatic rings in the molecular structure of PAGs, which enhances the hydrophobicity of the molecules. Consequently, they exhibit a stronger affinity for solvents with higher hydrophobicity, further diminishing their solubility in highly polar or protonic media.

2.3 Thermal stability

The thermal stability of PAGs is a critical factor determining their applicability in photoresist formulations, where typical pre-baking and PEB temperatures range from 85 °C to 130 °C. To systematically evaluate the thermal stability of PAGs **1a–1e**, TGA and DSC analyses were performed. Fig. 2a and S18 present the TGA and DSC curves for PAGs **1a–1e**, respectively, with corresponding thermal stability data summarized in Table S2. The experimental results demonstrate that the 5% weight loss temperature ($T_{5wt\%}$) for these PAGs ranges from 280 °C to 305 °C, while their melting points (T_m) fall between 160 °C and 216 °C, significantly higher than the typical baking temperatures used in photoresist processing. These findings confirm that all investigated PAGs exhibit excellent thermal stability, fully meeting the practical requirements for photoresist applications.

2.4 Photophysical properties

The acid generation in PAG occurs only when the molecule absorbs photons and transitions to an excited state, leading to chemical bond cleavage and acid production. Inadequate UV absorption at specific wavelengths will hinder effective acid generation. Therefore, UV absorption testing of PAGs is

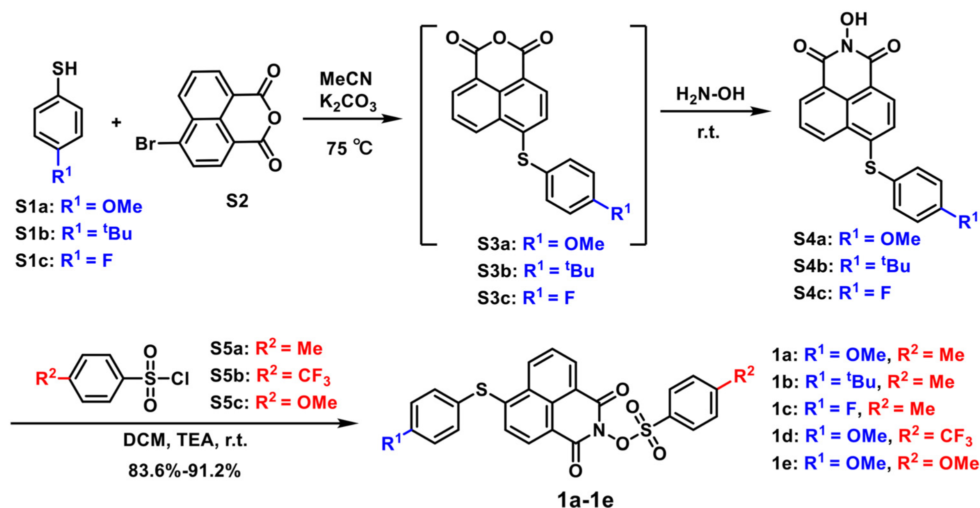

Scheme 1 Synthesis of nonionic sulfonate ester PAGs **1a–1e**.

Open Access Article. Published on 26 1404. Downloaded on 09/03/1405 12:12:44 ..
This article is licensed under a Creative Commons Attribution-NonCommercial 3.0 Unported Licence.

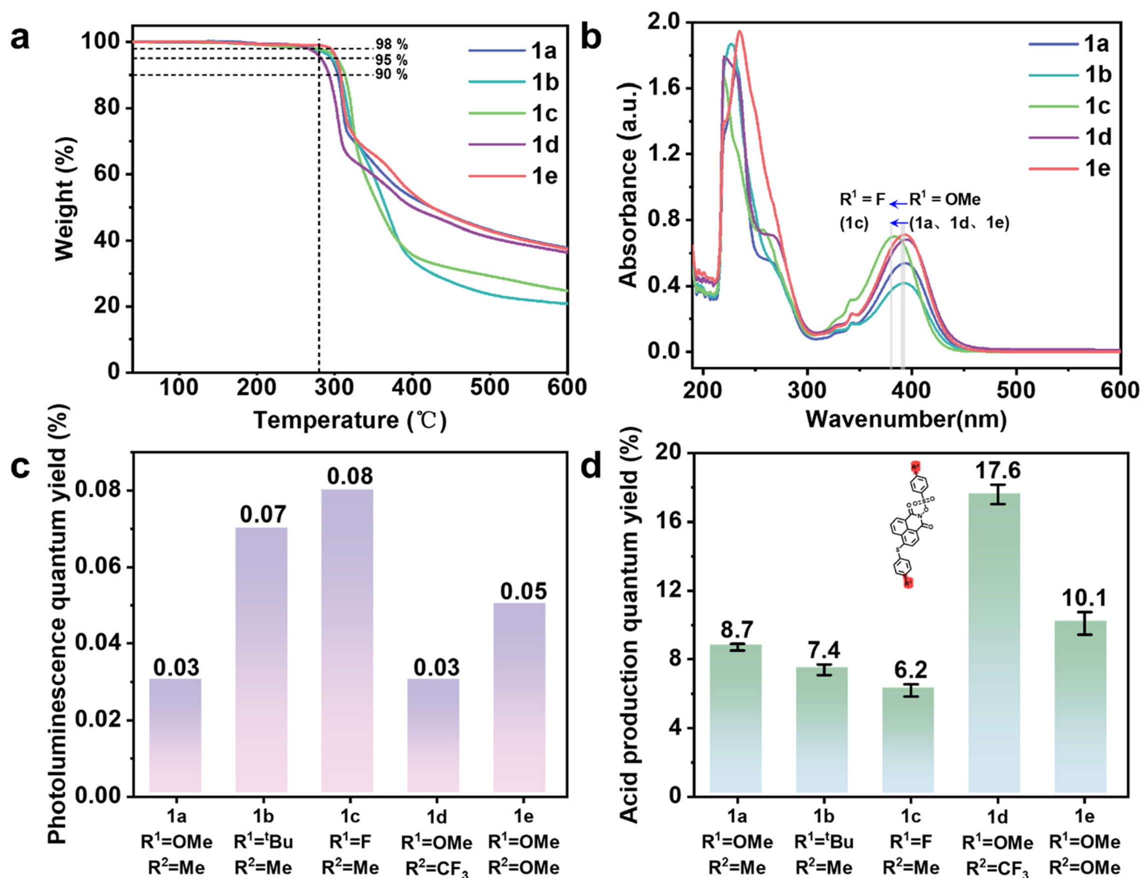

Fig. 2 (a) TGA curves, (b) UV-vis spectra, (c) Φ_p and (d) Φ_a of PAGs **1a–1e**.

crucial. Through UV-visible spectroscopy analysis of PAGs, the maximum absorption wavelength and suitable light source range can be determined. The UV absorption spectra of PAGs **1a–1e** were measured at a concentration of 2.0×10^{-5} M in acetonitrile as the solvent, as illustrated in Fig. 2b. Table S3 presents a summary of the primary UV absorption statistics, where λ_{max} indicates the wavelength of maximum absorption and ε represents the molar absorption coefficient. The results showed that PAGs **1a–1e** exhibit intense absorption bands near 220 nm, attributed to the π–π* transitions of the naphthalimide units in their molecular structure. Additionally, significant absorption is observed near 390 nm, which is characteristic of intramolecular charge transfer (ICT) between the electron-donating phenylthio units and the electron-withdrawing naphthalimide units. Notably, the substituent structure (Scheme 1, R^1) at the 4-position of the phenylthio unit significantly affects the ICT absorption peak. When the substituent is an electron-donating methoxy group (R^1 = OMe), the absorption peaks of PAGs **1a**, **1d**, and **1e** are essentially at the same position, whereas when the substituent is changed to an electron-withdrawing fluorine (R^1 = F), the absorption of PAG **1c** is markedly blueshifted by about 10 nm. The rigidity of the naphthalimide backbone ensures strong π-conjugation, while substituent-related intramolecular charge transfer demonstrates tunable optical properties through systematic structural modifications. To evaluate the potential application of PAGs **1a–1e** at critical lithography wavelengths, we examined their ε at 248 nm, 254 nm, and 365 nm, as detailed in Table 1. The results indicate that at these key wavelengths, the ε values of PAGs **1a–1e**

Table 1 Molecular structures, photophysical parameters, and pattern performance of PAGs **1a–1e**

PAG	Φ_p	254 nm		Pattern performance			
		Φ_a	I (W cm^{-2})	Photoresist	365 nm (min)	254 nm (min)	EBL (μC cm^{-2})
1a (R^1 = OMe, R^2 = Me)	0.03%	8.7%	8.27×10^{-4}	PR-**1a**	>1	7	485.4 ± 4.60
1b (R^1 = ^{t}Bu, R^2 = Me)	0.07%	7.4%	8.22×10^{-4}	PR-**1b**	>1	10	508.3 ± 5.40
1c (R^1 = F, R^2 = Me)	0.08%	6.2%	8.43×10^{-4}	PR-**1c**	>1	11	571.9 ± 11.45
1d (R^1 = OMe, R^2 = CF_3)	0.03%	17.6%	8.48×10^{-4}	PR-**1d**	30 s	2	54.4 ± 1.60
1e (R^1 = OMe, R^2 = OMe)	0.05%	10.1%	8.23×10^{-4}	PR-**1e**	>1	5	439.9 ± 6.45

© 2025 The Author(s). Co-published by the Institute of Process Engineering, Chinese Academy of Sciences and the Royal Society of Chemistry

Open Access Article. Published on 26 1404. Downloaded on 09/03/1405 12:12:44 ..
This article is licensed under a Creative Commons Attribution-NonCommercial 3.0 Unported Licence.

exceed 10^4 M^{-1} cm^{-1}. Therefore, all PAGs demonstrate significant potential for lithography applications at 248 nm, 254 nm, and 365 nm.

Based on the acid generation mechanism of PAGs, when excited molecules do not undergo dissociation but instead release energy through fluorescence, the efficiency of acid generation may be adversely affected. Consequently, the fluorescence spectra of the synthesized PAGs were evaluated. Fluorescence spectra of PAGs **1a–1e** were measured at a concentration of 2.0×10^{-5} M, using an excitation wavelength of 254 nm and acetonitrile as the solvent, as depicted in Fig. S19. The fluorescence spectra revealed that all PAGs exhibited weak fluorescence emission upon excitation at 254 nm. Additionally, the Φ_p of all PAG molecules were determined (Fig. 2c and Table 1). The Φ_p values for PAGs **1a–1e** were 0.03%, 0.07%, 0.08%, 0.03%, and 0.05%, respectively, indicating that the probability of these PAG molecules returning to the ground state *via* fluorescence emission is minimal. This low fluorescence emission favors bond cleavage and enhances Φ_a.

2.5 Acid generation quantum yield

Among the performance parameters of PAGs, the Φ_a is the most critical, as it directly impacts photoresist sensitivity. We accurately calculated the Φ_a of PAGs **1a–1e**, and the detailed test procedures can be found in the SI. As depicted in Fig. 2d and Table 1, the measured Φ_a values of PAGs **1a–1e** are 8.7%, 7.4%, 6.2%, 17.6%, and 10.1%, respectively, all of which are greater than the reported value of naphthalimide sulfonate PAG **13** (Φ_a = 4%) by Tsuguo Yamaoka's group.[46] The experimental results demonstrate that adjusting the electron-donating and electron-withdrawing abilities of the substituents (R^1 and R^2) on the naphthalimide–benzenesulfonate backbone can significantly influence the Φ_a of PAGs. When R^2 is fixed as methyl (Me, PAGs **1a–1c**), PAG **1a**, which possesses an electron-donating group (methoxy, OMe) at the R^1 position, exhibits the highest Φ_a (8.7%), outperforming PAG **1b** (R^1 = *tert*-butyl, ^{t}Bu, 7.4%) and PAG **1c** (R^1 = F, 6.2%). This indicates that when R^1 is an electron-donating group, it can enhance the electron density of the naphthalimide, promote charge separation upon photoexcitation, and thereby increase Φ_a. Conversely, when R^1 is fixed as methoxy (OMe, PAGs **1a**, **1d**, and **1e**), the introduction of a strong electron-withdrawing group (trifluoromethyl, CF_3) at the R^2 position in PAG **1d** achieves a significantly higher Φ_a (17.6%), far exceeding those of PAG **1a** (R^2 = Me, 8.7%) and PAG **1e** (R^2 = OMe, 10.1%). This suggests that when R^2 is an electron-withdrawing substituent, it can reduce the electron density of the benzenesulfonate moiety, destabilize the N–O bond, and thereby substantially increase Φ_a. The outstanding performance of PAG **1d** exemplifies an optimal D–π–A system, where the donor (R^1 = OMe) enhances the photosensitization ability, and the acceptor (R^2 = CF_3) facilitates efficient acid release, maximizing intramolecular charge transfer efficiency and achieving Φ_a. This establishes a clear structure–property relationship for designing high-performance PAGs through rational substituent engineering.

2.6 Theoretical calculations

FMO theory serves as a critical tool for elucidating the electronic and photophysical properties of organic compounds.[47,48] The calculation of FMO energy levels is essential for evaluating molecular photochemical processes and stability. The energy gap between the highest occupied molecular orbital (HOMO) and the lowest unoccupied molecular orbital (LUMO) reflects the charge transfer characteristics in excited states, with a larger HOMO–LUMO gap (ΔE) correlating with lower chemical reactivity.

Through systematic density functional theory (DFT) calculations on a series of PAGs **1a–1e** combined with experimental characterization, this study provides an in-depth understanding of the structure–activity relationship between molecular orbital energy levels, electronic transition properties, and Φ_a. The ground-state geometric structures of all molecules were optimized using the B3LYP/6-31G(d,p) method. Excited-state properties were calculated *via* time-dependent DFT (TD-DFT) at the B3LYP/6-311G(d,p) level, supplemented with FMO analysis and visualization using Multiwfn[49] and Visual Molecular Dynamics software (Fig. 3). Table 2 summarizes the data on the HOMO, LUMO, ΔE, cutoff wavelengths ($\lambda_{cutoff} = hc/\Delta E$), N–O bond lengths, and excitation energy of PAGs **1a–1e**. Computational results indicate that the ΔE of the PAGs shows a significant negative

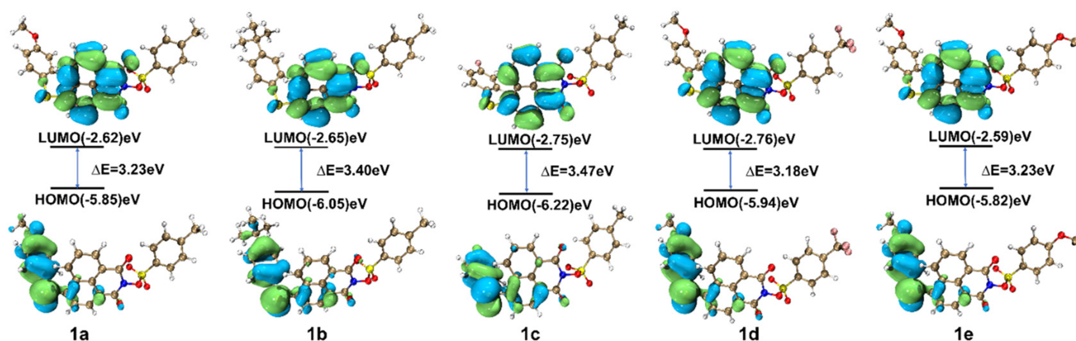

Fig. 3 Frontier molecular orbitals and their energies of PAGs **1a–1e** obtained by DFT calculations.

© 2025 The Author(s). Co-published by the Institute of Process Engineering, Chinese Academy of Sciences and the Royal Society of Chemistry

Open Access Article. Published on 26 1404. Downloaded on 09/03/1405 12:12:44 ..
This article is licensed under a Creative Commons Attribution-NonCommercial 3.0 Unported Licence.

Table 2 The calculated HOMO/LUMO energy levels, ΔE, λ_{cutoff}, N–O bond length and excitation energy of PAGs **1a–1e**

PAG	HOMO (eV)	LUMO (eV)	ΔE (eV)	λ_{cutoff} (nm)	BL_{N-O} (Å)	Excitation energy (eV)
1a (R^1 = OMe, R^2 = Me)	−5.85	−2.62	3.23	384	1.3738	3.6172
1b (R^1 = ^{t}Bu, R^2 = Me)	−6.05	−2.65	3.40	365	1.3738	3.6280
1c (R^1 = F, R^2 = Me)	−6.22	−2.75	3.47	357	1.3735	3.6471
1d (R^1 = OMe, R^2 = CF_3)	−5.94	−2.76	3.18	390	1.3747	3.6020
1e (R^1 = OMe, R^2 = OMe)	−5.82	−2.59	3.23	384	1.3737	3.6145

correlation with the experimentally measured Φ_a (determined under 254 nm irradiation). FMO analysis reveal that the LUMO is primarily localized on the naphthalimide core, while the HOMO mainly resides on the phenylthio moiety attached to the naphthalimide. Therefore, altering the electron-donating/electron-withdrawing ability of the substituent (R^1) at the 4-position of the phenylthio group can significantly influence the HOMO energy level of the PAG molecules, with relatively minor changes to the LUMO energy level. Specifically, when the substituent (R^1) is changed from the electron-donating methoxy group (OMe) to the electron-withdrawing fluorine atom (F), the HOMO energy level of PAG **1c** (−6.22 eV) is reduced by 0.37 eV, while its LUMO energy level (−2.75 eV) decreases by only 0.13 eV compared to those of PAG **1a** (HOMO/LUMO = −5.85/−2.62 eV). Consequently, compared to PAG **1a**, the ΔE of PAG **1c** widens by 0.24 eV, resulting in a lower Φ_a. On the other hand, modifying the substituent (R^2) at the 4-position of the phenylsulfonate unit influences both the HOMO and LUMO energy levels through inductive effects, with a more pronounced effect on the LUMO than on the HOMO. As a result, the ΔE of PAG **1d** (3.18 eV) is narrow relative to PAG **1e** (3.23 eV), resulting in a higher Φ_a. The λ_{cutoff} values of PAGs **1a–1e** show excellent correlation with the experimental UV absorption spectra in the 300–400 nm range. Notably, PAG **1d** has the longest N–O bond length (1.3747 Å), indicating a higher susceptibility to bond cleavage, which further supports its higher Φ_a (17.6%). Furthermore, the energy order of the strongest oscillator strength transition ($S_0 \rightarrow S_2$) is: **1d** (3.6020 eV) < **1e** (3.6145 eV) < **1a** (3.6172 eV) < **1b** (3.6280 eV) < **1c** (3.6471 eV). This order aligns perfectly with the experimental Φ_a measured at 254 nm, indicating that a lower excitation energy favors the initiation of the photochemical reaction. This result clarifies that rational design of the electronic properties of substituents R^1 and R^2 enables fine-tuning of the HOMO and LUMO energy levels, thereby influencing the energy gap and photochemical reactivity.

2.7 Lithographic performance

2.7.1 365 nm UV exposure. Due to the poor response of many existing PAGs to 365 nm UV light, they cannot be directly utilized for 365 nm lithography. Based on the absorption characteristics of PAGs **1a–1e** at 365 nm, these PAGs were blended with the polymer PG to prepare CAR photoresists PR-**1a**, PR-**1b**, PR-**1c**, PR-**1d**, and PR-**1e**, respectively. Subsequently, these five types of photoresists were exposed under a 365 nm light source with an exposure power of 50 mW cm^{-2} to investigate their suitability for 365 nm lithography and to examine the effect of different PAGs on the sensitivity of the photoresist.

Fig. 4 presents a comparative analysis of lithographic patterns obtained using different photoresists (PR-**1a** to PR-**1e**) under 365 nm exposure conditions. The most notable

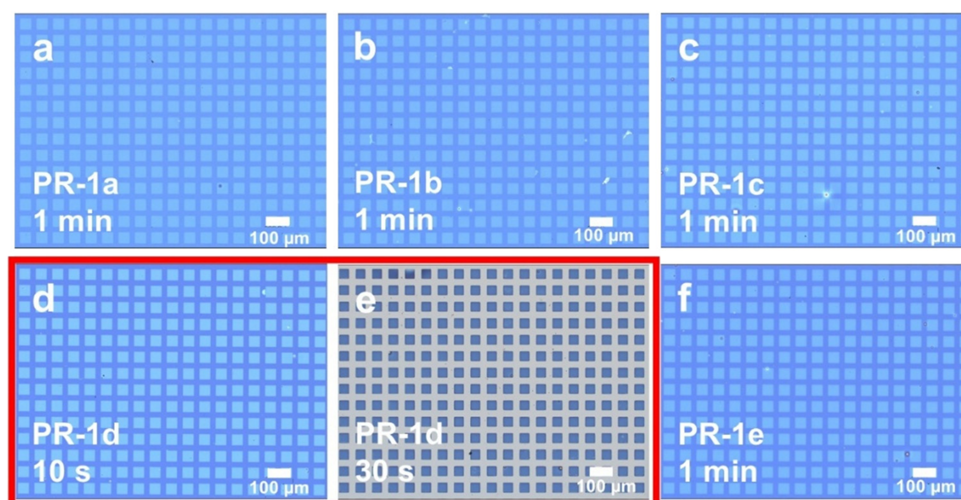

Fig. 4 Optical microscope images of lithographic patterns obtained with different photoresists using 365 nm. (a) PR-**1a**; (b) PR-**1b**; (c) PR-**1c**; (d and e) PR-**1d**; (f) PR-**1e**.

© 2025 The Author(s). Co-published by the Institute of Process Engineering, Chinese Academy of Sciences and the Royal Society of Chemistry

Open Access Article. Published on 26 1404. Downloaded on 09/03/1405 12:12:44 ..
This article is licensed under a Creative Commons Attribution-NonCommercial 3.0 Unported Licence.

observation is that PR-**1d** produces discernible pattern features within just 10 seconds (see Fig. 4d) and achieves a complete and clear lithographic pattern within 30 seconds (see Fig. 4e). This exceptional performance is directly correlated with the higher Φ_a of PAG **1d** (see Table 1). Additionally, lithographic patterns are observable in PR-**1a**, PR-**1b**, PR-**1c**, and PR-**1e** after an exposure time of 1 minute, indicating that PAGs **1a**–**1e** can be directly used in 365 nm lithography without the addition of sensitizers. This provides a new structural design strategy for PAGs suitable for 365 nm lithography and also offers new possibilities for further enhancing the performance of 365 nm photoresists.

2.7.2 254 nm UV exposure. Due to the stronger absorption of the five PAGs at 254 nm compared to 365 nm, the lithographic performance of the five blended photoresists PR-**1a**, PR-**1b**, PR-**1c**, PR-**1d**, and PR-**1e** under 254 nm illumination was further investigated. To minimize the influence of other factors on the performance of the photoresists, all lithographic process conditions were kept constant across each experimental group except for the exposure time, allowing for the study of the impact of the Φ_a of the five PAGs on their sensitivity.

As shown in Fig. 5, under a 254 nm light source with an exposure power of 0.8 mW cm^{-2}, the five photoresists (PR-**1a** to PR-**1e**) gradually revealed and fully developed the school emblem pattern with increasing exposure time. Notably, the exposure results demonstrate a clear correlation between the Φ_a of PAGs and the sensitivity of the photoresists. Optical micrographs reveal that PR-**1d** achieves complete pattern formation within just 2 minutes of exposure time (Fig. 5d)—the shortest among all formulations—indicating the highest sensitivity. This is followed by PR-**1e** (5 minutes), PR-**1a** (7 minutes), PR-**1b** (10 minutes), and PR-**1c** (11 minutes), respectively. This sensitivity ranking (PR-**1d** > PR-**1e** > PR-**1a** > PR-**1b** > PR-**1c**) perfectly aligns with the Φ_a trend of their respective PAG components (see Table 1), providing direct experimental evidence that enhanced acid generation efficiency translates to superior photoresist sensitivity. The highly sensitive patterning capability of PR-**1d** highlights its potential for high-throughput deep UV lithography applications. These results not only validate the structure–performance relationship between PAG design and photoresist performance, but also demonstrate the practical feasibility of these formulations in semiconductor manufacturing processes.

2.7.3 EBL. Currently, there have been no reports on the application of non-ionic PAGs in sub-30 nm lithography. To enhance the utility of these materials, this study investigates the lithographic performance of five photoresists PR-**1a**, PR-**1b**, PR-**1c**, PR-**1d**, and PR-**1e** under EBL. E_0 and contrast, as key parameters for evaluating photoresist performance, were determined based on the normalized remaining thickness under varying exposure doses (10–700 μC cm^{-2}). Fig. 6 presents the sensitivity curves and contrast performance of the five photoresists, with normalized thickness data detailed in Fig. S21–S25. The results reveal that PR-**1d** achieves exceptional lithographic performance, demonstrating the highest E_0 (54.4 μC cm^{-2})—a remarkable value compared to literature reports—and optimal contrast (γ = 24.39). The E_0 of the other photoresists follows the order: PR-**1e** (439.9 μC cm^{-2}), PR-**1a** (485.4 μC cm^{-2}), PR-**1b** (508.3 μC cm^{-2}) and PR-**1c** (571.9 μC cm^{-2}), which precisely correlates with the Φ_a trends of their respective PAG components (**1d** > **1e** > **1a** > **1b** > **1c**, see Table 1). This direct correlation further confirms that enhanced Φ_a translates to improved photoresist sensitivity. Furthermore, PR-**1d**'s superior contrast (γ = 24.39) indicates excellent dissolution selectivity between exposed and unexposed regions, highlighting its strong potential for high-resolution patterning applications.

The combined results from sensitivity and contrast measurements position PR-**1d** as a particularly promising candidate for advanced lithographic processes requiring both

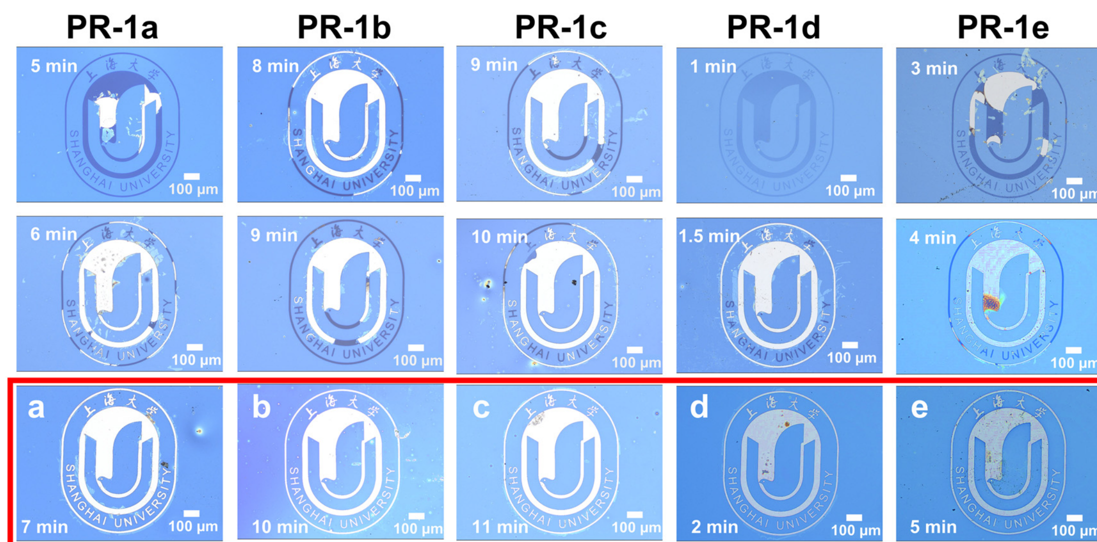

Fig. 5 Optical microscope images of lithographic patterns obtained at different exposure times for each photoresist under a 254 nm light source. (a) PR-**1a** (7 min); (b) PR-**1b** (10 min); (c) PR-**1c** (11 min); (d) PR-**1d** (2 min); (e) PR-**1e** (5 min).

© 2025 The Author(s). Co-published by the Institute of Process Engineering, Chinese Academy of Sciences and the Royal Society of Chemistry

Open Access Article. Published on 26 1404. Downloaded on 09/03/1405 12:12:44 ..
This article is licensed under a Creative Commons Attribution-NonCommercial 3.0 Unported Licence.

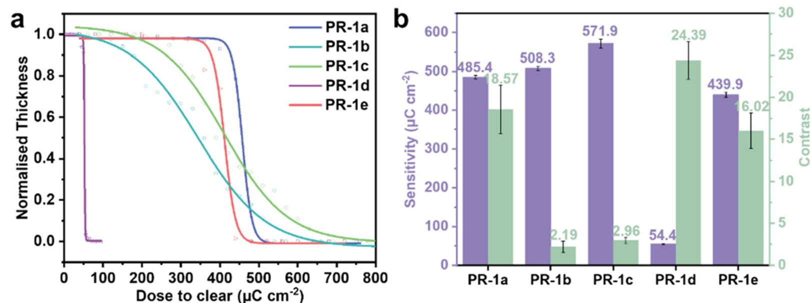

Fig. 6 (a) Sensitivity curves and (b) E_0 and contrast of the five photoresists.

high sensitivity and high resolution. Therefore, we further selected PR-**1d** for subsequent high-resolution line exposure experiments. Fig. 7 presents a comprehensive analysis of line/space (L/S) patterns fabricated with the PR-**1d** photoresist under optimized conditions, integrating SEM images with quantitative spatial distribution statistics. Fig. 7a–c, exposed at 160 μC cm^{-2},

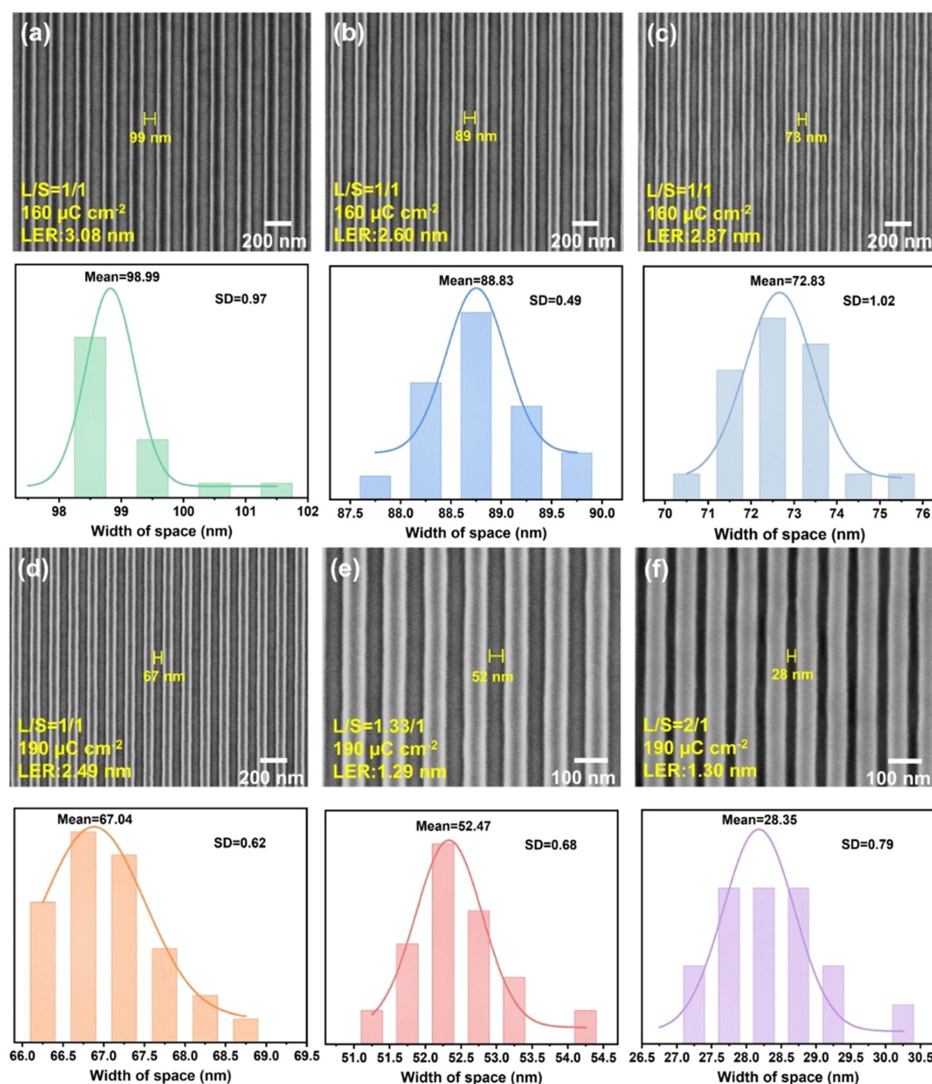

Fig. 7 SEM images and normal distribution analysis of line/space (L/S) patterns with varying line widths fabricated using the PR-**1d** photoresist *via* EBL. (a) Actual critical dimension (ACD) = 99 nm (target critical dimension (TCD) = 100 nm, L/S = 1/1); (b) ACD = 89 nm (TCD = 90 nm, L/S = 1/1); (c) ACD = 73 nm (TCD = 80 nm, L/S = 1/1); (d) ACD = 67 nm (TCD = 70 nm, L/S = 1/1); (e) ACD = 52 nm (TCD = 60 nm, L/S = 2/1); (f) ACD = 28 nm (TCD = 30 nm, L/S = 2/1) (PEB at 110 °C for 30 s and development in TMAH for 60 s).

© 2025 The Author(s). Co-published by the Institute of Process Engineering, Chinese Academy of Sciences and the Royal Society of Chemistry

Open Access Article. Published on 26 1404. Downloaded on 09/03/1405 12:12:44 ..
This article is licensed under a Creative Commons Attribution-NonCommercial 3.0 Unported Licence.

exhibit resolutions of 99 nm (LER = 3.08 nm), 89 nm (LER = 2.60 nm), and 73 nm (LER = 2.87 nm), respectively. Moreover, Fig. 7d–f, exposed at 190 μC cm^{-2}, show higher resolutions of 67 nm (LER = 2.49 nm), 52 nm (LER = 1.29 nm), and 28 nm (LER = 1.30 nm), respectively. The histogram quantifies the spacing distribution, revealing that all patterns exhibit narrowly defined normal distributions. The calculated average values of the voids based on normal distribution analysis are 98.99 nm, 88.83 nm, 72.83 nm, 67.04 nm, 52.47 nm, and 28.35 nm, respectively, with corresponding standard deviations (SDs) of 0.97, 0.49, 1.02, 0.62, 0.68, and 0.79, respectively. Additionally, a clear dependence of the patterned space width on the exposure dose was observed in Fig. S26, confirming the dose as a key parameter for dimensional control in the CAR. Notably, even at the 28 nm resolution with a small LER value of 1.3 nm (Fig. 7f), the standard deviation remains as low as 0.79. These results conclusively demonstrate that PR-**1d** achieves both high resolution (28 nm) and exceptional uniformity (SD < 1) in nanopatterning. To objectively evaluate the performance of this work in the context of similar studies, we have provided Table S5 in the SI, which systematically compares the key performance parameters of the PAGs and corresponding photoresists reported in this study with those described in the recent literature. The analysis demonstrates that the advantages of our work are reflected in two aspects: systematically, this study covers a comprehensive performance evaluation ranging from molecular design and photophysical properties (such as Φ_a) to 365 nm/254 nm lithography and EBL, whereas most reports focus only on individual aspects. In terms of performance, the developed photoresist not only exhibits multi-wavelength compatibility, but also achieves a high resolution of 28 nm (compared to the 50–90 nm resolution typical of most reported nonionic PAG-based CARs) and a low LER of 1.30 nm (*versus* approximately 3.5 nm for similar materials) under EBL. These key metrics significantly outperform those reported in the existing literature, demonstrating the strong competitiveness of this material for high-end patterning applications.

Through multi-mode characterization *via* Atomic Force Microscopy (AFM), the nanoscale patterning performance of the PR-**1d** photoresist under different electron beam exposure doses was systematically investigated (Fig. 8). At the lower dose (110 μC cm^{-2}, Fig. 8a), the two-dimensional morphology revealed blurred line edges, with a measured space width of 55 nm, indicating incomplete pattern development. The three-dimensional topography displayed irregular and sharp nanostructures. Although the sidewall inclination angle was relatively large, the overall structure height was significantly insufficient. Line profile analysis confirmed a height variation of only about 20 nm, far below the initial photoresist film thickness (approximately 90 nm), demonstrating insufficient photoacid generation efficiency under this condition, which led to incomplete development of the pattern. Under the optimized dose (160 μC cm^{-2}, Fig. 8b), the patterning quality was significantly enhanced. The two-dimensional morphology showed clear, complete, and uniform line/space structures, with a measured space width of 95 nm that closely matched the design target (minor

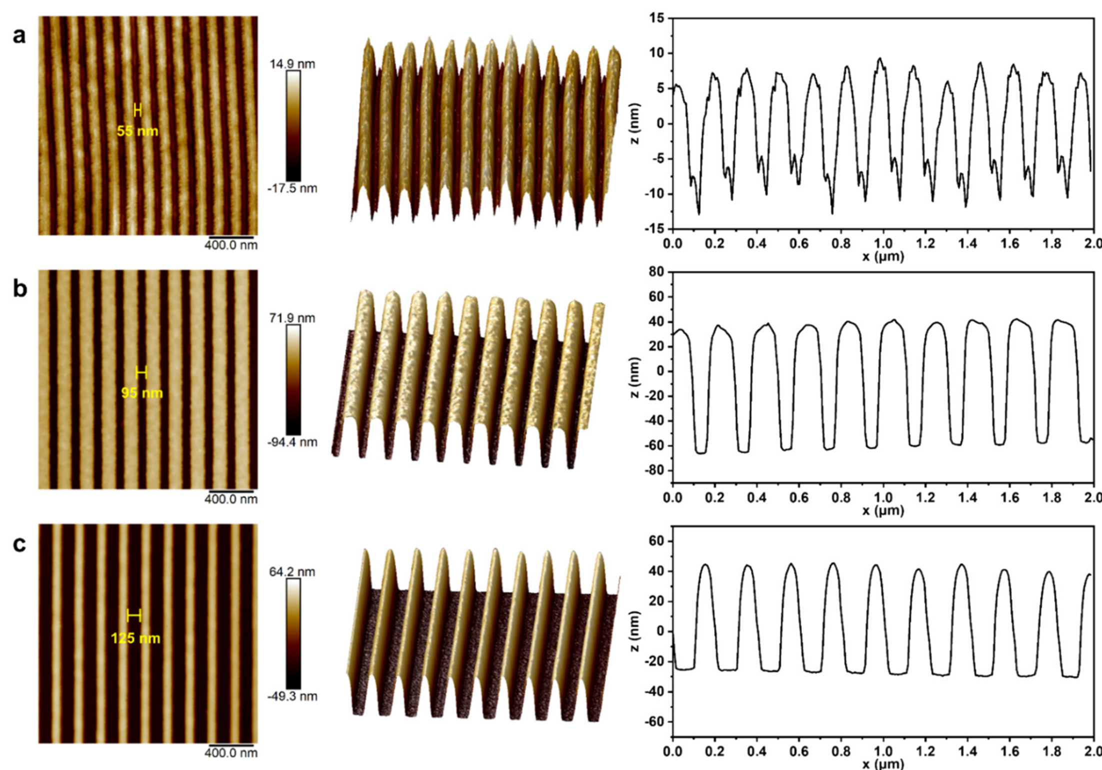

Fig. 8 AFM multidimensional analysis to investigate the patterning performance of the PR-**1d** photoresist at exposure doses of (a) 110 μC cm^{-2}, (b) 160 μC cm^{-2}, and (c) 210 μC cm^{-2} (from left to right: 2D morphology, 3D view, and line profile height curve; layout pattern: 100 nm L/S).

Open Access Article. Published on 26 1404. Downloaded on 09/03/1405 12:12:44 ..
This article is licensed under a Creative Commons Attribution-NonCommercial 3.0 Unported Licence.

deviations may originate from AFM tip convolution effects). The three-dimensional view further confirmed features with a high aspect ratio, steep sidewall morphology, and flat top surface. Line profile analysis indicated nearly vertical sidewall angles and well-controlled feature dimensions, achieving high-fidelity linewidth patterning. At the excessive dose (210 μC cm^{-2}, Fig. 8c), although the two-dimensional morphology maintains the overall continuity of the pattern, overexposure causes excessive diffusion of the photoacid, resulting in significant graphic distortion and ultimately leading to a space width of 125 nm. The three-dimensional topography exhibited top surface erosion, reduced structure height, and edge rounding. Line profile results further confirmed the presence of top loss and linewidth shrinkage, indicating loss of critical dimension control due to overexposure. The study results demonstrate that the PR-**1d** photoresist, at the optimized dose, can simultaneously achieve high resolution, good sidewall morphology and structural uniformity in patterning performance. In addition, we performed AFM multimodal characterization on the patterns of the PR-**1d** photoresist at smaller feature sizes (Fig. S27). The measurement results show that even if the feature size is further reduced, all patterns still maintain good morphology quality: the visible contour of the two-dimensional morphology image is clear and complete, without obvious edge roughness or fracture phenomenon. The 3D view further indicates that the structure has a high aspect ratio and shape fidelity, with sharp pattern edges and steep sidewalls. The quantitative display of uniform structure height through line profile analysis further confirms the potential application of the PR-**1d** photoresist in advanced lithography.

Fig. 9 presents the lithographic process flow of the photoresist used in this study and its photochemical imaging mechanism.[23,25,34] The photoresist film consists of polymer bearing acid-labile groups and PAGs. Upon exposure to 254 nm/365 nm/EBL, the PAGs absorb energy and reach an excited state, leading to the cleavage of their N–O bond. This homolytic dissociation generates radical pairs, which subsequently abstract protons from the surrounding environment to produce a strong acid. During the PEB step, the generated acid acts as a catalyst, triggering deprotection of the acid-labile groups on the polymer backbone. This reaction converts hydrophobic groups into hydrophilic carboxylic groups, rendering the exposed regions soluble in an alkaline developer. The acid is then regenerated, propagating a chain reaction and markedly improving efficiency. Finally, during development using a 2.38 wt% tetramethylammonium hydroxide (TMAH) aqueous solution, the chemically transformed exposed regions are dissolved and removed, while the unexposed areas remain, thereby forming clear positive-tone spatial patterns on the substrate. From the lithographic imaging mechanism, it is evident that the acid-generation efficiency of the PAG is the most critical factor governing resist sensitivity: the higher the Φ_a, the higher the lithographic sensitivity. In this study, PAG **1d** features electron-withdrawing groups (–CF_3) at the *para* position of the benzene sulfonate units and an electron-donating group (–OMe) at the *para* position of the phenylthio substituent located at the 4-position on the naphthalimide backbone. It exhibited the highest Φ_a (17.6%) and therefore showed markedly higher E_0 (54.4 μC cm^{-2}) than the other PAGs.

3 Conclusions

This study designed and synthesized five nonionic PAGs based on the naphthalimide–benzenesulfonate backbone, and systematically investigated their solubility, thermal stability, photophysical properties, Φ_p, Φ_a, and lithographic performance. The experimental results demonstrate that PAGs **1a–1e** exhibit excellent solubility in common photoresist solvents and

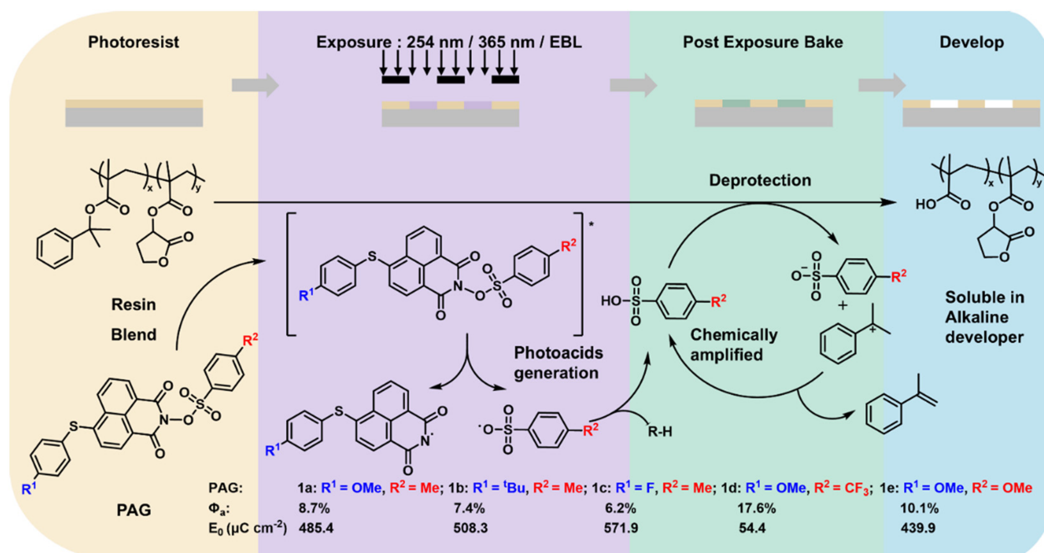

Fig. 9 Overview of the lithography process and photosensitive imaging mechanism of the photoresist.

© 2025 The Author(s). Co-published by the Institute of Process Engineering, Chinese Academy of Sciences and the Royal Society of Chemistry

Open Access Article. Published on 26 1404. Downloaded on 09/03/1405 12:12:44 ..
This article is licensed under a Creative Commons Attribution-NonCommercial 3.0 Unported Licence.

remarkable thermal stability, fully meeting lithographic processing requirements. The UV spectra demonstrate that the optical properties of the PAG can be adjusted by structural modifications. Φ_a measurements established a clear structure–property relationship for PAGs, where the superior performance of PAG **1d** (Φ_a = 17.6%) reflects the optimal D–π–A system, in which the synergistic combination of electron-donating and electron-withdrawing groups enhances photosensitivity, while an electron-withdrawing substituent efficiently releases the acid, thereby achieving a high acid generation quantum yield. DFT calculations further confirm that the established structure–property relationship provides a solid foundation for the molecular engineering of PAG molecules with high Φ_a. Our comprehensive evaluation demonstrates that all five PAG-based positive-tone photoresists successfully achieve high-quality patterning across multiple lithographic platforms (365 nm, 254 nm, and EBL), with their sensitivity performance directly correlating with the Φ_a values of PAGs. Notably, the PR-**1d** formulation containing PAG **1d** demonstrated exceptional performance in EBL evaluation, showing both the highest sensitivity (E_0 = 54.4 μC cm^{-2}) and achieving an industry-leading resolution of 28 nm at a 190 μC cm^{-2} exposure dose, representing state-of-the-art performance for nonionic PAG-based resists. This work provides fundamental insights into the structure–property relationships of nonionic sulfonate PAGs, as well as demonstrates their potential for sub-30 nm lithography applications and making them a promising resist for advanced node semiconductor fabrication.

4 Experimental section

4.1 Photoresist preparation and spin-coating procedures

The polymer (poly(2-phenyl-2-propyl methacrylate-*co*-γ-butyrolactone-3-yl methacrylate), PG[43]) (47.5 mg) and PAG (5 mmol) were dissolved in 2 ml DCE and filtered twice through a 0.1 μm polytetrafluoroethylene membrane filter to prepare the photoresist solution. The silicon substrates were first pretreated with hexamethyldisilazane (HMDS) in an HMDS-6090 system at 150 °C for 600 s.[50] The photoresist solution was then spin-coated onto the pretreated substrates at 2000 rpm or 6000 rpm for 60 s, resulting in film thicknesses of 180 ± 7 nm and 90 ± 5 nm, respectively. The coated substrates are then pre-baked at 90 °C for 60 s. The 180 nm-thick films are exposed to 365 nm or 254 nm UV light, while the 90 nm-thick films are patterned *via* EBL.

4.2 Lithography experiment

The wafer was exposed to 365 nm, 254 nm, or EBL (using a CABL-9500C system operating at an acceleration voltage of 50 kV and a beam current of 100 pA). After exposure, the wafer was placed in a post-exposure bake (PEB) for 30 s at 110 °C. Subsequently, a 2.38 wt% tetramethylammonium hydroxide (TMAH) aqueous solution was used to develop it for 60 s followed by rinsing with water for 60 s and blowing with nitrogen gas.

Author contributions

Changchang Zhuang was responsible for the synthesis of photoresist materials, the design of experiments, and the drafting of the manuscript. Jiao Chen was responsible for the synthesis of photoacid generators, organized the data and contributed to the writing and editing of the manuscript. Tao Wang participated in the EBL experiments. Jun Zhao offered guidance for the EBL experiments. Haoyuan Li provided financial support. Hanshen Xin and Jianhua Zhang provided financial support, supervised the experiments and revised the manuscript.

Conflicts of interest

The authors declare no conflict of interest.

Data availability

The data supporting this article have been included as part of the Supplementary information. Supplementary information: the SI contains additional experimental data, methodological details, and supporting figures referenced in the main text. See DOI: https://doi.org/10.1039/d5im00286a.

Acknowledgements

The authors thank the BL08U1B beamline of the Shanghai Synchrotron Radiation Facility for providing the EBL. The National Natural Science Foundation of China (grant numbers: 22090013) and the Shanghai Committee of Science and Technology (grant number: YDZX20213100002672 and 21QA1402900) provided financial support for this study.

References

1 C. K. Ober, F. Käfer and C. Yuan, Recent developments in photoresists for extreme-ultraviolet lithography, *Polymer*, 2023, **280**, 126020.

2 X. Wang, P. Tao, Q. Wang, R. Zhao, T. Liu, Y. Hu, Z. Hu, Y. Wang, J. Wang and Y. Tang, Trends in photoresist materials for extreme ultraviolet lithography: A review, *Mater. Today*, 2023, **67**, 299–319.

3 H. Xu, V. Kosma, E. P. Giannelis and C. K. Ober, In pursuit of Moore's Law: Polymer chemistry in action, *Polym. J.*, 2018, **50**, 45–55.

4 M. Li and E. Aqad, Key Challenges and opportunities for advanced extreme ultraviolet lithography photoresist materials, *Adv. Funct. Mater.*, 2025, **35**, 2420962.

5 H. Chen, W. Li, Y. Zhao, X. Huang, J. Zhang, P. Ji, J. Zhao, P. Chen and X. Peng, Hybrid alkyl-ligand tin-oxo clusters for enhanced lithographic patterning performance via intramolecular interactions, *Ind. Chem. Mater.*, 2025, **3**, 543–552.

6 R. Peng, P. Lian, J. Chen, T. Yu, Y. Zeng, S. Wang, X. Guo, R. Hu, J. Zhao, Y. Wu, G. Yang and Y. Li, Lithographic performances of aryl sulfonate ester-modified polystyrenes

Open Access Article. Published on 26 1404. Downloaded on 09/03/1405 12:12:44 ..
This article is licensed under a Creative Commons Attribution-NonCommercial 3.0 Unported Licence.

as nonchemically amplified resists, *Ind. Chem. Mater.*, 2025, **3**, 553–566.

7 H. Ito, Dissolution behavior of chemically amplified resist polymers for 248-, 193-, and 157-nm lithography, *IBM J. Res. Dev.*, 2001, **45**, 683–695.

8 H. Ito, Chemical amplification resists: Inception, implementation in device manufacture, and new developments, *J. Polym. Sci., Part A: Polym. Chem.*, 2003, **41**, 3863–3870.

9 H. I. H. Ito, Advances in chemical amplification resist systems, *Jpn. J. Appl. Phys.*, 1992, **31**, 4273.

10 E. Reichmanis, F. Houlihan, O. Nalamasu and T. Neenan, Chemical amplification mechanisms for microlithography, *Chem. Mater.*, 1991, **3**, 394–407.

11 E. Reichmanis, F. Houlihan, O. Nalamasu and T. Neenan, Chemically amplified resists: Chemistry and processes, *Adv. Mater. Opt. Electron.*, 1994, **4**, 83–93.

12 H. Ridaoui, A. Dirani, O. Soppera, E. Ismailova, C. Brochon, G. Schlatter, G. Hadziioannou, R. Tiron, P. Bandelier and C. Sourd, Chemically amplified photoresists for 193-nm photolithography: Effect of molecular structure and photonic parameters on photopatterning, *J. Polym. Sci., Part A: Polym. Chem.*, 2010, **48**, 1271–1277.

13 S. L. Ablaza, J. F. Cameron, G. Xu and W. Yueh, The effect of photoacid generator structure on deep ultraviolet resist performance, *J. Vac. Sci. Technol., B: Microelectron. Nanometer Struct.–Process., Meas., Phenom.*, 2000, **18**, 2543–2550.

14 C. M. Bottoms, T. Terlier, G. E. Stein and M. Doxastakis, Ion diffusion in chemically amplified resists, *Macromolecules*, 2021, **54**, 1912–1925.

15 S.-Y. Moon and J.-M. Kim, Chemistry of photolithographic imaging materials based on the chemical amplification concept, *J. Photochem. Photobiol., C*, 2007, **8**, 157–173.

16 M. Shirai and H. Okamura, i-Line sensitive photoacid generators for UV curing, *Prog. Org. Coat.*, 2009, **64**, 175–181.

17 M. Shirai and M. Tsunooka, Photoacid and photobase generators: Chemistry and applications to polymeric materials, *Prog. Polym. Sci.*, 1996, **21**, 1–45.

18 Y. Zhang, H. Yu, L. Wang, X. Wu, J. He, W. Huang, C. Ouyang, D. Chen and B. E. Keshta, Advanced lithography materials: From fundamentals to applications, *Adv. Colloid Interface Sci.*, 2024, **329**, 103197.

19 H. Wu and K. Gonsalves, Novel positive-tone chemically amplified resists with photoacid generator in the polymer chains, *Adv. Mater.*, 2001, **13**, 670–672.

20 Q. Wang, C. Yan, F. You and L. Wang, A new type of sulfonium salt copolymers generating polymeric photoacid: Preparation, properties and application, *React. Funct. Polym.*, 2018, **130**, 118–125.

21 M. Wang, N. D. Jarnagin, C.-T. Lee, C. L. Henderson, W. Yueh, J. M. Roberts and K. E. Gonsalves, Novel polymeric anionic photoacid generators (PAGs) and corresponding polymers for 193 nm lithography, *J. Mater. Chem.*, 2006, **16**, 3701–3707.

22 M. Wang, W. Yueh and K. E. Gonsalves, Novel ionic photoacid generators (PAGs) and corresponding PAG bound polymers, *J. Photopolym. Sci. Technol.*, 2007, **20**, 751–755.

23 J. Deng, S. Bailey, S. Jiang and C. K. Ober, High-performance chain scissionable resists for extreme ultraviolet lithography: Discovery of the photoacid generator structure and mechanism, *Chem. Mater.*, 2022, **34**, 6170–6181.

24 T. Tsuchimura, Recent progress in photo-acid generators for advanced photopolymer materials, *J. Photopolym. Sci. Technol.*, 2020, **33**, 15–26.

25 Y. Liu, D. Wang, H. Wang, H. Chen, Q. Wang and W. Kang, Enhanced lithography performance with imino/imido benzenesulfonate photoacid generator-bound polymer resists, *Small*, 2025, **21**, 2412297.

26 N. Zivic, P. K. Kuroishi, F. Dumur, D. Gigmes, A. P. Dove and H. Sardon, Recent advances and challenges in the design of organic photoacid and photobase generators for polymerizations, *Angew. Chem., Int. Ed.*, 2019, **58**, 10410–10422.

27 C. J. Martin, G. Rapenne, T. Nakashima and T. Kawai, Recent progress in development of photoacid generators, *J. Photochem. Photobiol., C*, 2018, **34**, 41–51.

28 R. A. Lawson and C. L. Henderson, Mesoscale simulation of molecular resists: The effect of PAG distribution homogeneity on LER, *Microelectron. Eng.*, 2009, **86**, 741–744.

29 W. Xu, T. Li, G. Li, Y. Wu and T. Miyashita, Novel polymeric nonionic photoacid generators and corresponding polymer Langmuir-Blodgett (LB) films for photopatterning, *J. Photochem. Photobiol., A*, 2011, **219**, 50–57.

30 N. A. Kuznetsova, G. V. Malkov and B. G. Gribov, Photoacid generators. Application and current state of development, *Russ. Chem. Rev.*, 2020, **89**, 173.

31 Y. Liu, D. Wang, Q. Wang and W. Kang, Polymerizable nonionic perfluorinated photoacid generators for high-resolution lithography, *Small Methods*, 2024, **8**, 2400112.

32 C. J. Martin, G. Rapenne, T. Nakashima and T. Kawai, Recent progress in development of photoacid generators, *J. Photochem. Photobiol., C*, 2018, **34**, 41–51.

33 E. Torti, G. Della Giustina, S. Protti, D. Merli, G. Brusatin and M. Fagnoni, Aryl tosylates as non-ionic photoacid generators (PAGs): Photochemistry and applications in cationic photopolymerizations, *RSC Adv.*, 2015, **5**, 33239–33248.

34 L. Zhang, B. Feng, S. Pang, H. Xin, K. Li and Y. Jin, Synthesis and performance study of nonionic photoacid generators based on Norbornene-imide, *J. Mol. Struct.*, 2024, **1304**, 137653.

35 Y. Wang, G. Sheng, J. Xie, D. Wan and M. Jin, Push–pull biphenyl–based iodonium salts: Highly sensitive one-component photoinitiators for photopolymerization under UV–visible LEDs, *Prog. Org. Coat.*, 2024, **188**, 108209.

36 Q. Sun, B. Feng, Z. Sun, R. Liu, H. Ding and Y. Jin, Synthesis and properties of a series of sulfonate ester photoacid generators, *React. Chem. Eng.*, 2024, **9**, 630–641.

37 J. Andraos, G. Barclay, D. Medeiros, M. Baldovi, J. Scaiano and R. Sinta, Model studies on the photochemistry of phenolic sulfonate photoacid generators, *Chem. Mater.*, 1998, **10**, 1694–1699.

38 T. Endo, S. Suzuki, N. Miyagawa and S. Takahara, Multifunctional photo acid generator for fluorescence imaging based on self-contained photoreaction, *J. Photochem. Photobiol., A*, 2008, **200**, 181–186.

© 2025 The Author(s). Co-published by the Institute of Process Engineering, Chinese Academy of Sciences and the Royal Society of Chemistry

39 M. Ikbal, R. Banerjee, S. Atta, D. Dhara, A. Anoop and N. P. Singh, Synthesis, photophysical and photochemical properties of photoacid generators based on N-hydroxyanthracene-1, 9-dicarboxyimide and their application toward modification of silicon surfaces, *J. Org. Chem.*, 2012, **77**, 10557–10567.

40 E. Torti, S. Protti, D. Merli, D. Dondi and M. Fagnoni, Photochemistry of N-arylsulfonimides: An easily available class of nonionic photoacid generators (PAGs), *Chemistry*, 2016, **22**, 16998–17005.

41 J.-P. Malval, F. Morlet-Savary, X. Allonas, J.-P. Fouassier, S. Suzuki, S. Takahara and T. Yamaoka, On the cleavage process of the N-trifluoromethylsulfonyloxy-1, 8-naphthalimide photoacid generator, *Chem. Phys. Lett.*, 2007, **443**, 323–327.

42 M. Oelgemoeller and W. H. Kramer, Synthetic photochemistry of naphthalimides and related compounds, *J. Photochem. Photobiol., C*, 2010, **11**, 210–244.

43 Z. Changchang, C. Jiao, W. Tao, Z. Jun, L. Haoyuan, X. Hanshen and Z. Jianhua, Anionic photoacid generator bound polymer photoresists with improved performance for advanced lithography patterning, *J. Appl. Polym. Sci.*, 2024, **142**, e56622.

44 L.-Y. Peng, S.-L. Xiang, J.-D. Huang, Y.-Y. Ren, P. Hong, C. Li, J. Liu and M.-Q. Zhu, Dual nonionic photoacids synergistically enhanced photosensitivity for chemical amplified resists, *Chem. Eng. J.*, 2024, **482**, 148810.

45 L. T. Zhou, Z. X. Tang, H. Y. Li, H. S. Xin and J. H. Zhang, Enhancing 365 nm photoresist performance using 2-isopropylthioxanthone as a photosensitizer, *ACS Appl. Mater. Interfaces*, 2025, **17**, 39542–39551.

46 J.-P. Malval, S. Suzuki, F. Morlet-Savary, X. Allonas, J.-P. Fouassier, S. Takahara and T. Yamaoka, Photochemistry of naphthalimide photoacid generators, *J. Phys. Chem. A*, 2008, **112**, 3879–3885.

47 I. Shafiq, I. Amanat, M. Khalid, M. A. Asghar, R. Baby, S. Ahmed and S. M. Alshehri, Influence of azo-based donor modifications on nonlinear optical amplitude of D-π-A based organic chromophores: A DFT/TD-DFT exploration, *Synth. Met.*, 2023, **297**, 117410.

48 M. Khalid, A. Ali, R. Jawaria, M. A. Asghar, S. Asim, M. U. Khan, R. Hussain, M. F. ur Rehman, C. J. Ennis and M. S. Akram, First principles study of electronic and nonlinear optical properties of A–D–π–A and D–A–D–π–A configured compounds containing novel quinoline–carbazole derivatives, *RSC Adv.*, 2020, **10**, 22273–22283.

49 T. Lu, A comprehensive electron wavefunction analysis toolbox for chemists, Multiwfn, *J. Chem. Phys.*, 2024, **8**, 082503.

50 T. Wang, C. Zhuang, G. Yang, H. Xin, L. Jiang and J. Zhang, Interface engineering of underlayer of chemically-amplified EUV photoresists to enhance the photolithographic performance, *Mater. Sci. Eng., B*, 2024, **307**, 117539.

Open Access Article. Published on 26 1404. Downloaded on 09/03/1405 12:12:44 ..
This article is licensed under a Creative Commons Attribution-NonCommercial 3.0 Unported Licence.